GE5228 Project Report

Spatio-temporal Analysis of Air Quality Dynamics and Urban Heat Island effects during the COVID-19

Group 2

Liu Weiyu

Wang Jifei

Xu Yuanyuan

Sun Tong

2020/10/31

Contents

LIST OF FIGURES

LIST OF TABLES

ABSTRACT

The outbreak of novel coronavirus pneumonia is the most serious global issue in 2020, causing enormous impacts on various aspects of human society from public health to economic growth. The ecological environment has also been affected due to the transformation of human activities during the epidemic period. The implementation of the 'Lockdown' and 'Stay-at-Home' policies have reduced the pollution emissions from transport and commercial areas, thus altered the urban environment. Based on the analysis of the temporal and spatial distribution of the COVID-19 cases, we studied the changes of the air and thermal environment in Wuhan City and New York City in 2020. Combining spatial interpolation and spatial clustering analysis, we further analyzed the dynamics of air pollution and Urban Heat Island (UHI) effect to evaluate environmental variations.

1. Introduction

1.1 Background

The novel coronavirus pneumonia (COVID-19), which broke out in Wuhan in January and was characterized as a global pandemic on March 11, spreads rapidly during the past nine months and has caused significant impacts on public health, economy, environment, and social interaction. COVID-19 is a long-standing challenge facing the human race and remains as a highlighted public health problem. Previous scientific research focused on the geospatial and spatial-statistical analysis of COVID-19 pandemic. The themes of disease mapping vary from spatiotemporal analysis, social and environmental geography, data mining and web-based geo-analysis (Franch et al., 2020).

Among the research papers that investigate the presence of spatial autocorrelation of COVID-19, the Moran's Index was primarily used to map the distribution of epidemic infection cases, and researchers made predictions via logistic model in the early study (Kang et al.,2020; Huang et al., 2020). The spatial features of disease transmission were explored based on social media data as well, using Kernel Density Analysis and Ordinary Least Square regression (Peng et al.,2020). More factors were taken into consideration to understand the spatial patterns of COVID-19. And the cluster analysis was applied to evaluate the contextual factors (Cordes et al., 2020).

Air quality is a vital indicator in environmental restoration and climate change study. According to Daniella et al., air quality has developed across 50 cities during the lockdown period (R-U Daniella et al., 2020). They made a global analysis of air quality and population correlation using $PM_{2.5}$ concentration data and studied the variations before and after quarantine. And Liane et al. analysed data from air quality stations in Brazil to assess air pollutant concentration variations during the partial lockdown (Nakada et al., 2020).

Urban Heat Island (UHI) is a micro-climate phenomenon in which urban areas have higher surface temperatures than the surrounding rural areas (Zhang et al., 2017). The main cause of UHI effect is the modification of urban configuration due to accelerating urbanization and the increasing anthropogenic activities. The magnitudes of the UHI effect are closely correlated with socio-economic growth and population increase. In UHI studies, two kinds of data are

2

widely applied in the assessment and quantification of the UHI effect. Traditionally, air temperature data provided by in-situ stations have the limitation of spatial coverage. With the development of remote sensing techniques, land surface temperature (LST) data derived from satellite images turn into the primary data source used in the surface UHI (SUHI) studies for its data availability and high spatial resolution (Yang et al., 2019). Urban thermal characteristic is one significant part of the urban environment monitoring. During COVID-19, the restriction of human activities changed the global restoration of climate elements such as air quality and temperature. Many existing papers explain the air quality improvement on a local or global scale. However, limited research is related to urban thermal dynamics change in the pandemic period. As one of the most important weather-related factor, LST can be used to evaluate further the impact of COVID-19 on urban environment (Mukherjee et al., 2020).

Most research regarding COVID-19 focused on the prediction and spatial distribution of the disease based on published data. Few studies made a statistical analysis of the socio-ecological and environmental consequences of the epidemic disease. The mitigation of pandemic influences requires global real-time statistical research and multiscale follow-up surveys with proactive planning and international solidarity. The interdisciplinary analysis of impacts caused by COVID-19 is essential to examine the policy of health interventions and controls as well as to provide a long-term plan for social life-style rehabilitation, economic recovery and environmental protection.

1.2 Objectives

To investigate the consequences of epidemic control strategies and understand the environmental changes during the disease outbreak, we focused our research on two typical cities, Wuhan City and New York City, which are both epicentres in the global pandemic. The primary purpose of our project is to make a temporal and spatial comparison of air pollution (i.e. PM2.5) and thermal environment variations (i.e. land surface temperature) in the metropolitan urban area. Using geospatial analysis tools and remote sensing data, we further explore the consequences of COVID-19 based on the distribution characteristics of disease mapping.

The objectives of our project are summarized as follows:
1) To understand the temporal and spatial distribution of COVID-19 cases in the two cities during the outbreak.
2) To assess the influence of epidemic spread based on the air quality level using critical air quality indicators, e.g. PM2.5, NO_2, CO, SO_2, O_3.
3) To investigate the spatial patterns of air pollutants and understand the Urban Heat Island phenomenon under the impact of COVID-19 spread.

2. Data and Method
2.1 Study Area
Wuhan City, located in Hubei Province, was the earliest outbreak region in China. The Yangtze River flows through the center of the city, dividing the central urban area of Wuhan into three regions. The city has a population of over 11 million and underwent a lockdown from January

23 to April 8. Until September 8, there were 68,139 cases in total in Wuhan during the epidemic outbreak (Peng et al., 2020). The geospatial location of Wuhan is 113°41'20"E ~ 115°6'40"E, 29°58'30" ~ 31°20'25".

New York City, located at the southern tip of the U.S state of New York, became the center of the epidemic at the end of March 2020. New York City has a highly dense population of 8.3 million people spread across five boroughs interconnected by a subway system that also extends into neighboring areas (U.S. Census Bureau, 2020). According to the New York City had 445,071 cases as of September 8, 2020. The geospatial location of New York City is 73°41'50"W ~ 74°15'25"W, 40°29'30"S ~ 40°55'10"S.
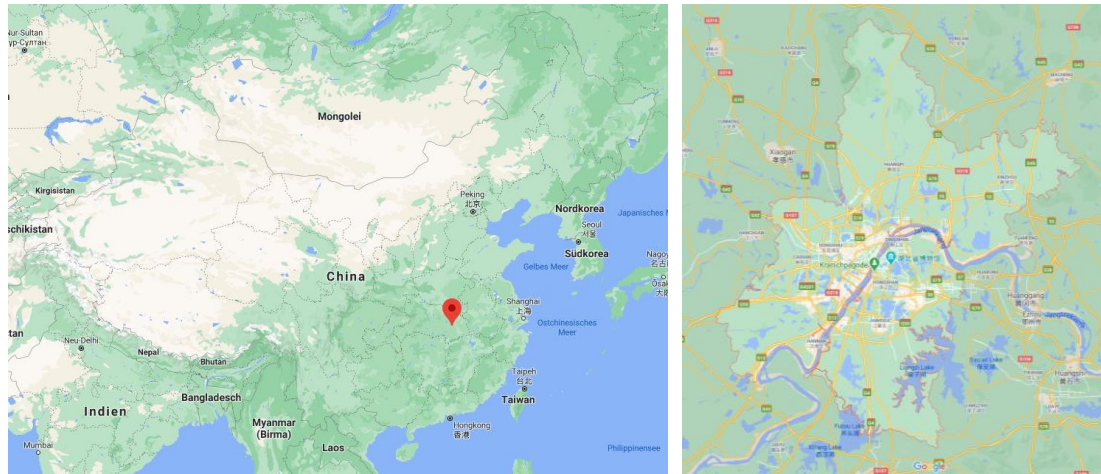
(a)The location of Wuhan City in China
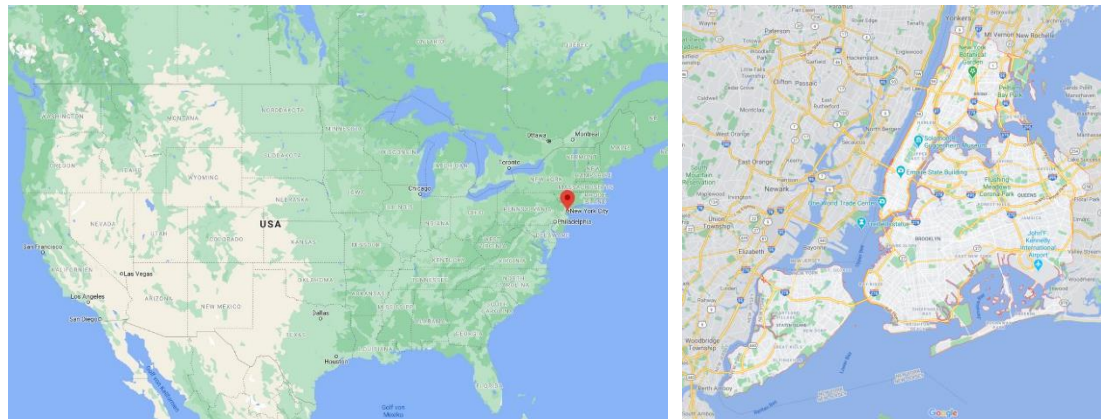
(b)The location of New York City in United States

Figure 2.1: Geographical location of the study area (Source: Google map)

2.2 Data

In our project, the comprehensive analysis of various environmental factors influenced by COVID-19 control strategies is based on multi-source data:

- The COVID-19 cases, population composition, and hospital assistance data.
- The daily air quality data of the Wuhan City and New York City.
- Satellite imagery data covers the study area

The COVID-19 data for Wuhan is accumulated from the Wuhan Health Commission website, and the New York data is from NYC Health website. The COVID-19 cases data in Wuhan is collected from 23rd Jan to 28th May, while the cases data in New York City is from 1st Mar to 17th Jun. The daily AQI data of Wuhan, from 1 January 2016 to 31 September 2020, is provided by the China National Environmental Monitoring Centre. The daily AQI data of New York, from 1 January 2016 to 31 September 2020, is provided by the United States Environmental Protection Agency (EPA).

The Landsat 8 satellite images for the year 2019, 2020 are provided by the U.S. Geological Survey (USGS). Due to the limitation of image quality and vacancy of data, we selected the image with little cloud cover over the study area before and after the pandemic outbreak. The Landsat 8 satellite comprises the camera of the Operational Land Imager (OLI) and the Thermal Infrared Sensor (TIRS) which can be used to study earth surface temperature and is used to study global warming (Li et al., 2020). In this study, we used Landsat8 Level L1B data to calculate Land Surface Temperature (LST) to monitor the dynamics of Urban Heat Island (UHI).

Table 2.1: The Data Source

Data	Wuhan	Website
COVID-19	Wuhan Municipal Health Commission	http://wjw.wuhan.gov.cn/xwzx_28/
Air quality data	China National Environmental Monitoring	http://www.cnemc.cn/
Satellite imagery	USGS	https://glovis.usgs.gov/app
Data	New York City	Website
COVID-19	NYC Health	https://www1.nyc.gov/site/doh/covid/covid-19-
Air quality data	United Stated Environmental Protection	https://www.epa.gov/outdoor-air-quality-data
Satellite imagery	USGS	https://glovis.usgs.gov/app

Table 2.2: The collected time of Landsat 8 OLI/TIRS images data

Location	Collected Time	
	2019	2020
Wuhan China	2019/03/10	2020/02/09
	2019/06/14	2020/04/13
	2019/08/01	2020/08/03
	2019/10/20	2020/10/22
New York City U.S.	2019/02/19	2020/03/09
	2019/04/24	2020/05/12
	2019/05/26	2020/06/13
	2019/06/27	2020/10/03

2.3 Methodology

The temporal analysis of COVID-19 cases and air quality factors is conducted in Excel using the available data. The spatial analysis is based on the platform ArcGIS Desktop and Pro.

2.3.1 *Spatial autocorrelation algorithm*

Moran's I statistic measures the spatial autocorrelation and is calculated as follows:

$$I = \frac{n \sum_{i,j} W_{ij}(Y_i - \bar{Y})(Y_j - \bar{Y})}{\sum_{i \neq j} W_{ij} \sum_i (Y_i - \bar{Y})^2} \tag{1}$$

where i and j were the region indexes and W_{ij} indicated the adjacency between area i and area j. This study considered different types of adjacency newly confirmed cases in areas i and j, respectively, and Y was the average of the number of newly confirmed cases in the entire region. A value of 0 indicated that there was no spatial autocorrelation in the data. A positive Moran's I value indicated the clustering of similar values, whereas a negative Moran's I value indicated the clustering of dissimilar values. The larger the absolute Moran's I value, the stronger the spatial autocorrelation (Kang et al., 2020).

2.3.2 Cluster analysis model

Hotspot analysis

The Hot Spot Analysis tool calculates the Getis-Ord Gi* statistic for each feature in a dataset. The resultant z-scores and p-values tell you where features with either high or low values cluster spatially. This tool works by looking at each feature within the context of neighbouring features. A feature with a high value is interesting but may not be a statistically significant hot spot (Andy, M., 2005). The hotspots of COVID-19 positive cases are mapped using Getis-Ord Gi* statistic algorithm to find the cluster patterns of disease outbreak and spread.

Cluster and Outlier Analysis (Anselin Local Moran's I)

Based on Moran's I statistic, the Cluster and Outlier Analysis tool identifies spatial clusters of features with high or low values. A positive value for I indicates that a feature has neighbouring features with similarly high or low attribute values; this feature is part of a cluster. A negative value for I indicates that a feature has neighbouring features with dissimilar values; this feature is an outlier. In either instance, the p-value for the feature must be small enough for the cluster or outlier to be considered statistically significant (Anselin, Luc, 1995).

2.3.3 Spatial interpolation method

Ordinary kriging is a geostatistical interpolation method base on spatially dependent variance, which used to find the best linear unbiased estimate(Belkhiri, Tiri, & Mouni, 2020). The general form of Ordinary kriging equation can be written as :

$$Z(x_p) = \sum_{i=1}^{n} \lambda_i Z(x_i) \tag{2}$$

In order to achieve unbiased estimations in kriging the following set of equations should be solved simultaneously:

$$\sum_{i=1}^{n} \lambda_i r(x_i, y_i) - \mu = r(x_i, x_p) \ where \ j = 1, \dots, n \ with \sum_{i=1}^{n} \lambda_i = 1 \tag{3}$$

Where $Z(x_p)$ is the estimated value of variable Z at location x_p; $Z(x_i)$ is known value at location x_i; λ_i is the weight associated with the data; μ is the Lagrange coefficient; $r(x_i, x_j)$ is the value of variogram corresponding to a vector with origin in x_i and extremity in x_j; and n is the number of sampling points used in estimation.

2.3.4 LST retrieval algorithm

Urban Heat Island is one of the most typical anthropogenic environmental characteristics in the urban area, During COVID-19 spread. The lockdown and 'stay-at-home' protocols changed the tracks and forms of human activity. Therefore, the urban environment is altered from both social and geographical aspects. To discover the vague change of urban ecology under anti-pandemic regulations, we collected temporal Landsat 8 OLI/TIRS images to evaluate the Land surface Temperature (LST) change between 2019 and 2020.

At present, there are mainly three surface temperature inversion algorithms: atmospheric correction method (also known as Radiative Transfer Equation, RTE), single-channel algorithm

and split-window algorithm. In this study, the LST retrieval process is based on atmospheric correction method, using Landsat8 TIRS inversion of surface temperature. First, the atmospheric effect on the surface thermal radiation is estimated and then subtracted from the total amount of thermal radiation observed by satellite sensors to obtain the surface thermal radiation intensity, which is then converted to the corresponding surface temperature.

The specific implementation is as follows: the thermal infrared radiation brightness value L_λ received by the satellite sensor is composed of three parts: atmospheric upwelling radiation brightness $L^\uparrow$, the true radiation brightness of the ground reaches the energy of the satellite sensor after passing through the atmosphere and the energy reflected by the atmosphere as it radiates down to the ground (Wang et al., 2016)..

By building Radiative Transfer Equation, the LST is obtained from the following expression:

$$L_{sensor,i} = \left[\varepsilon_i B_i(T_s) + (1 - \varepsilon_i)L^\downarrow_{atm,i}\right]\tau_i + L^\uparrow_{atm,i} \tag{4}$$

$$B_i(T_s) = \frac{L_{sensor,i} - L^\uparrow_{atm,i}}{\tau_i \varepsilon_i} - \frac{1 - \varepsilon_i}{\varepsilon_i} L^\downarrow_{atm,i} \tag{5}$$

$$T_s = \frac{c_2}{\lambda}[\ln\left(\frac{c_1}{\lambda^5 B_i(T_s)} + 1\right)]^{-1} \tag{6}$$

where L_{sensor} is the at-sensor radiance or Top of Atmospheric (TOA) radiance, i.e., the radiance measured by the sensor, $B_i(T_s)$ is the blackbody radiance of channel i, τ_i and ε_i are the atmospheric transmittance and land surface emissivity of channel i, and the $L^\uparrow_{atm,i}$ and $L^\downarrow_{atm,i}$ are the atmospheric upwelling and downwelling radiance of channel i, respectively, c_1 and c_2 are the Planck's radiation constants, for TIRS Band 10 data, the values is $774.89\ W/\mu m \cdot m^2 \cdot sr$ and $1321.08\ K$, respectively, λ is wavelength. The atmospheric parameters τ_i, $L^\uparrow_{atm,i}$ and $L^\downarrow_{atm,i}$ can be calculated from in situ radio soundings and using a radiative transfer codes like MODTRAN.
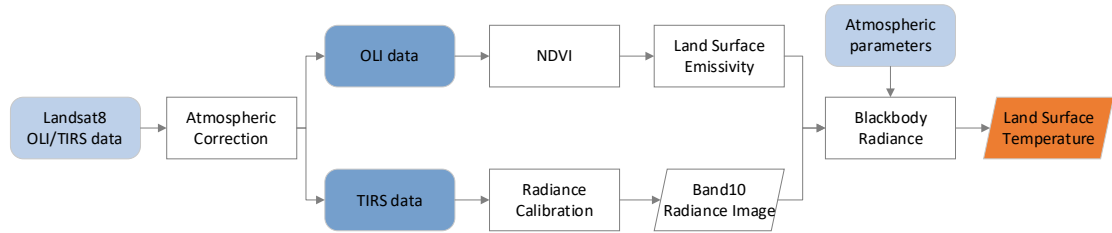

Figure 2.2: Flowchart for LST retrieval algorithm

3. Results and Analysis

In an attempt to assess the correlation of COVID-19 and environmental consequences, we conducted a statistical analysis and detection of environmental dynamics using measurable variables. The indicators we chose are typical factors that are affected by the consequences of pandemic spread. The qualitative analysis experiment was performed on the datasets to study the changing trend and statistical characteristics. Our analysis results include the following visualised products:

1) Maps of monthly distribution of COVID-19 cases.
2) Graphs of daily concentration change of air pollutants.
3) The temporal land surface temperature maps.

3.1 COVID-19 cases spatial analysis

3.1.1 COVID-19 cases distribution in China and the U.S.

Spatial patterns

According to the up-to-date data of total cases in China and the United States, the epidemic spread trend in these two countries has different features. China has controlled the epidemic spread within Hubei province since April 2020, whereas the U.S. is still under stressful coronavirus impacts. Most cases in China concentrate in Hubei province and Hongkong. Since Wuhan is the original outbreak city of COVID-19 in China, the death and positive cases mainly distributed in the urban area of Wuhan City. In the case of the New York State in the U.S., the cases accumulated in several counties. New York City, as one of the earliest regions in the U.S. hit by COVID-19, has an enormous number of the infected population.
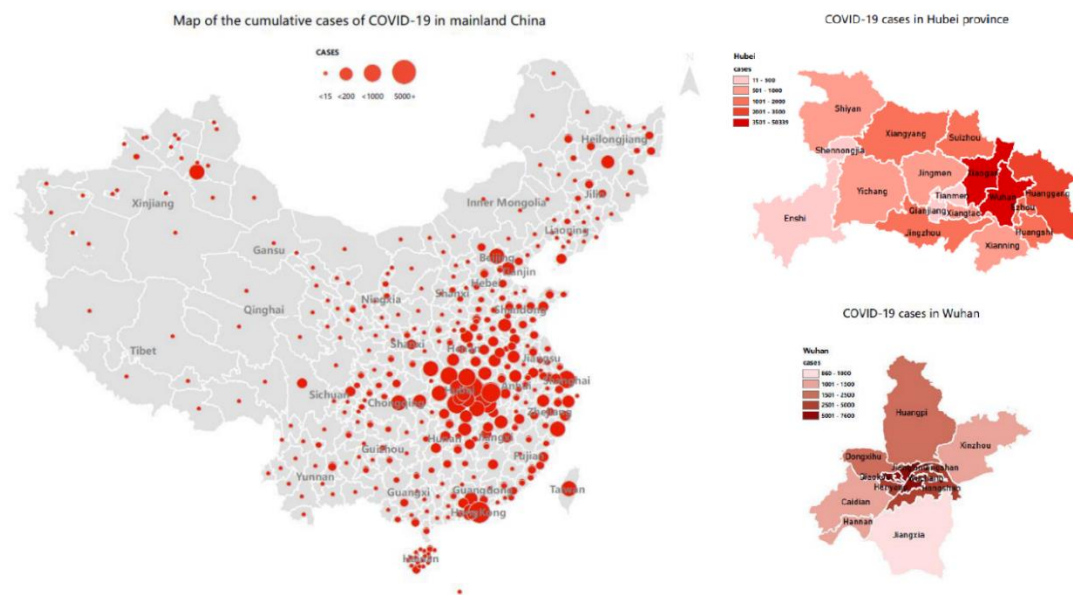

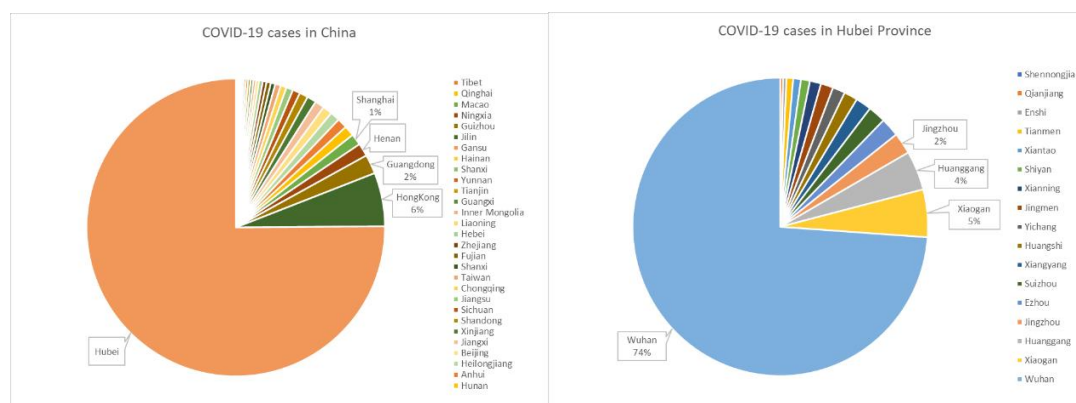Figure 3.1: COVID-19 total cases in mainland China, Hubei province and Wuhan City (Oct 10, 2020)

Figure 3.2: Pie charts of COVID-19 cases distribution in mainland China and Hubei province.
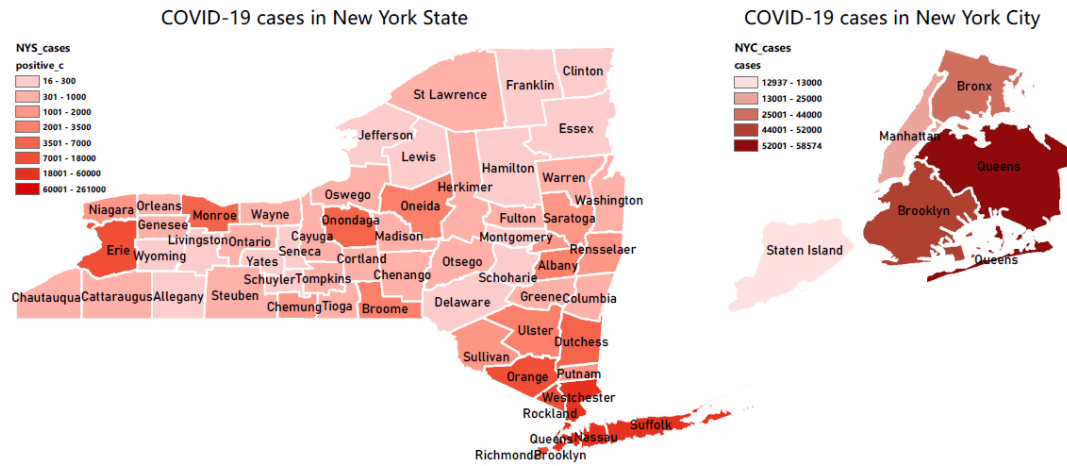
8

Figure 3.3: COVID-19 total cases in New York State, New York City, U.S. (Oct 10, 2020)
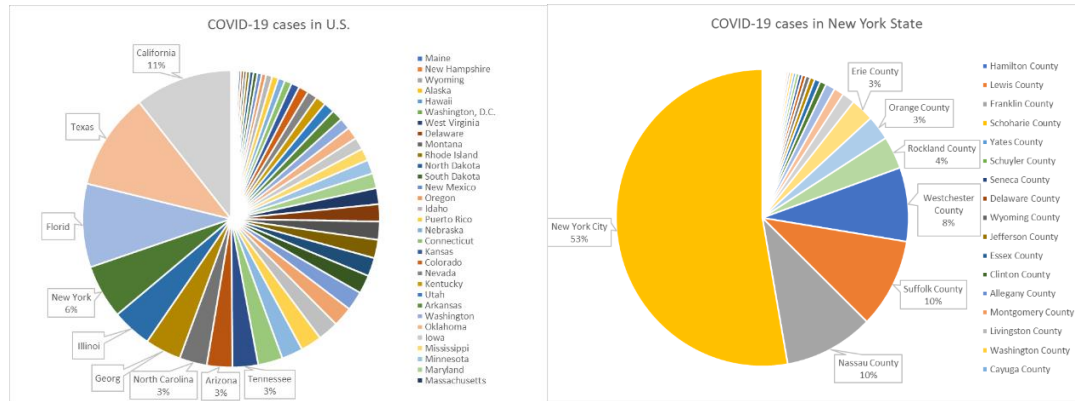

Figure 3.4: Pie charts of COVID-19 cases distribution in U.S. and New York State

Autocorrelation analysis

In our experiment, the spatial autocorrelation of COVID-19 cases between cities has been estimated through Moran'I index by using the formula (1). The values of Moran coefficients are around the interval of [0, 1], since there is a positive correlation among the confirmed cases according to the geographical structure, and its spatial distribution has prominent agglomeration characteristics. The increase of confirmed pneumonia cases in one region will inevitably lead to the increasing cases in adjacent areas, which means that a positive spill-over effect occurs. Thus, regions adjacent to COVID-19 hotspots are at higher risk.
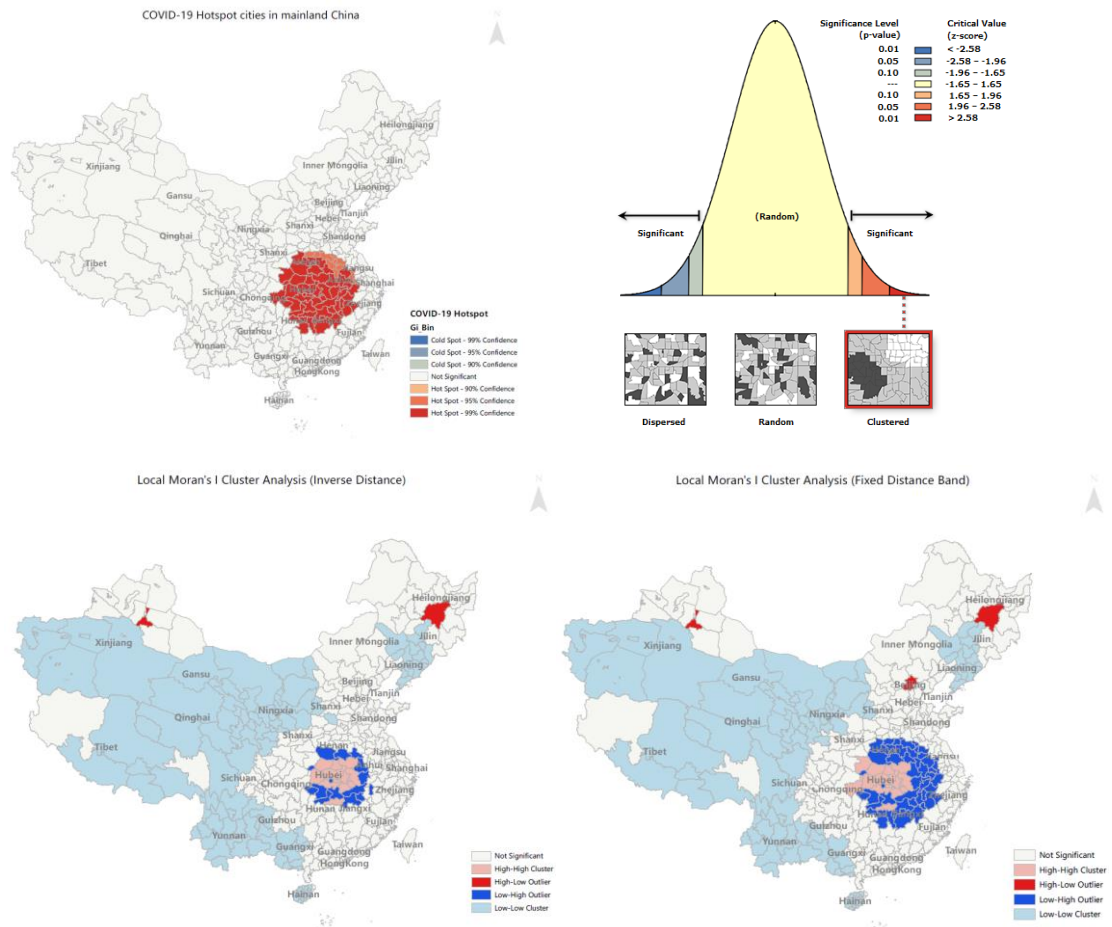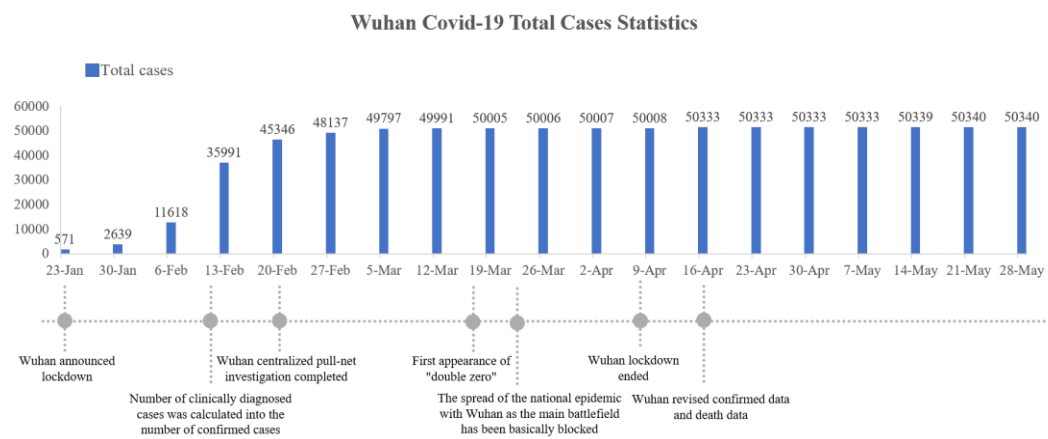
Figure 3.5: Cluster analysis of COVID-19 cases in mainland Chin

3.1.2 COVID-19 cases analysis in Wuhan City

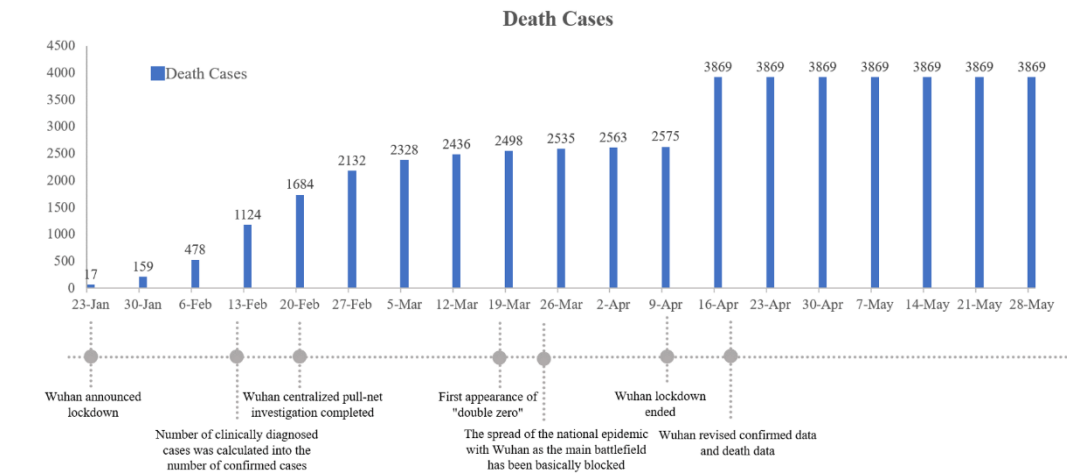Wuhan Covid-19 Total Cases Statistics

Figure 3.6: Time series plot of newly confirmed COVID-19 cases, and death cases in Wuhan
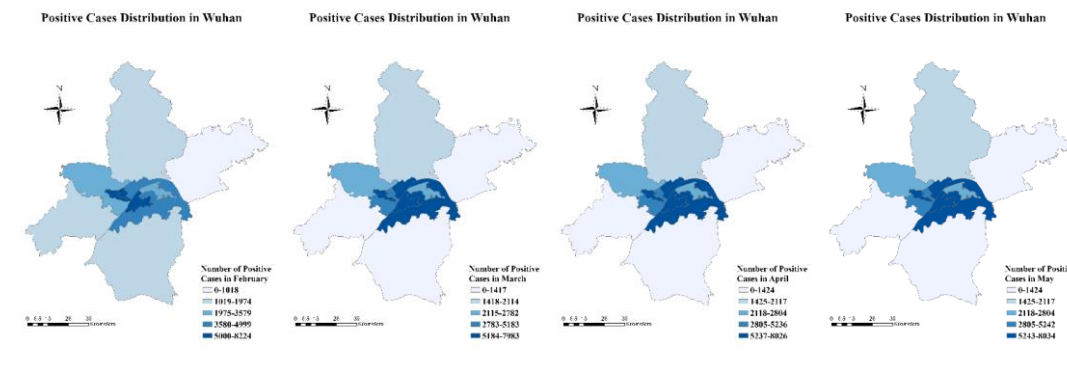

Figure 3.7: Positive cases distribution in Wuhan (February, March, April, May)

The COVID-19 pandemic originated with a cluster of mysterious, suspected pneumonia cases in the city of Wuhan, the capital of Hubei, China in December 2019. The potential disease outbreak soon drew nationwide attention. On 23rd January 2020, the government announced lockdown order in Wuhan City. By 29th January, the virus spread to all provinces of mainland China(Yuan, Li, 28 January 2020). The number of cases increased rapidly in February until the pandemic was under control in early March. By the time Wuhan ended lockdown order, over 2,575 died from the coronavirus infection-associated pneumonia, and 50,008 were confirmed to have been infected in Wuhan City.

The outbreak started from the urban districts and gradually spread to the suburban and rural areas across the disease pandemic periods. There were significant geographic differences in rates of confirmed cases, with the highest rates in the urban districts such as Jiangan, Jianghan, Qiaokou and Wuchang districts.

3.1.3   COVID-19 cases analysis in New York City
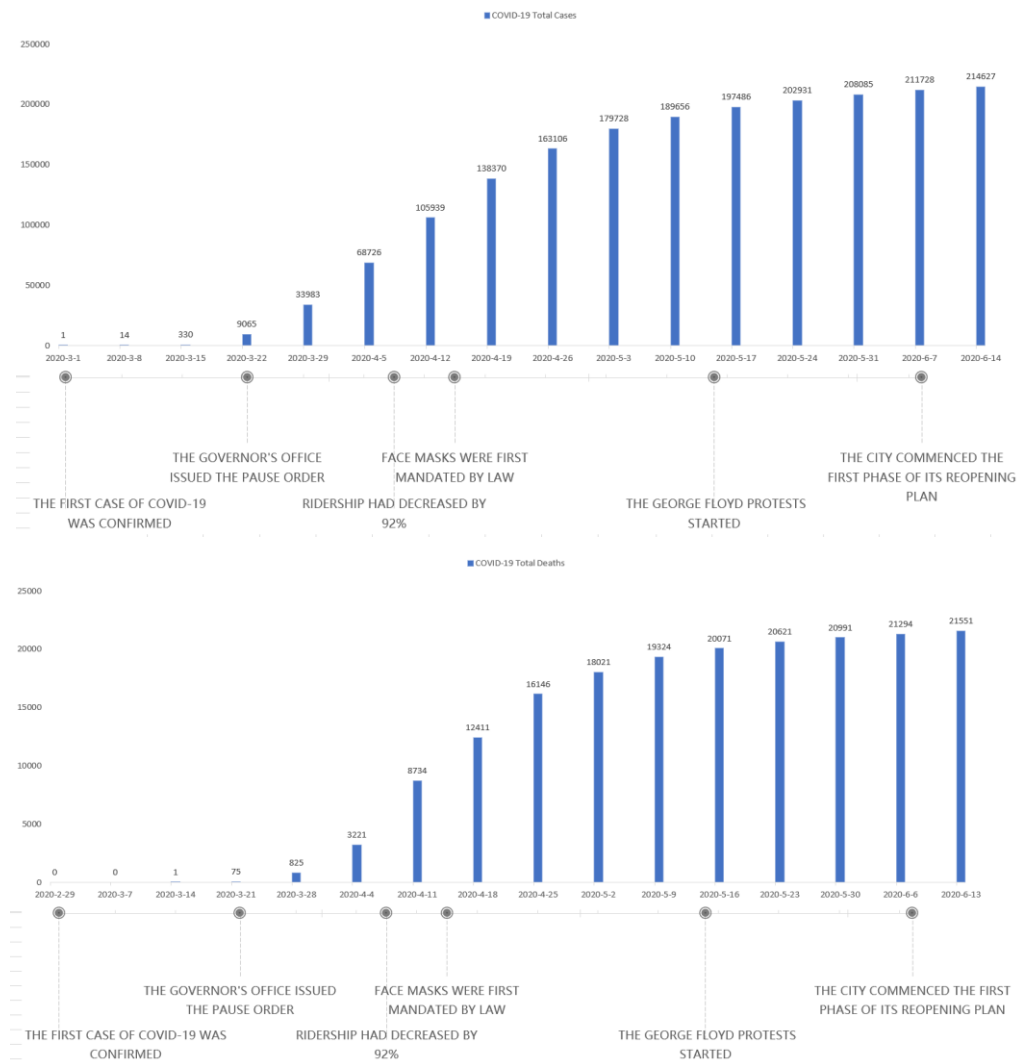

Figure 3.8: Time series plot of newly confirmed COVID-19 cases, and death cases in New York City
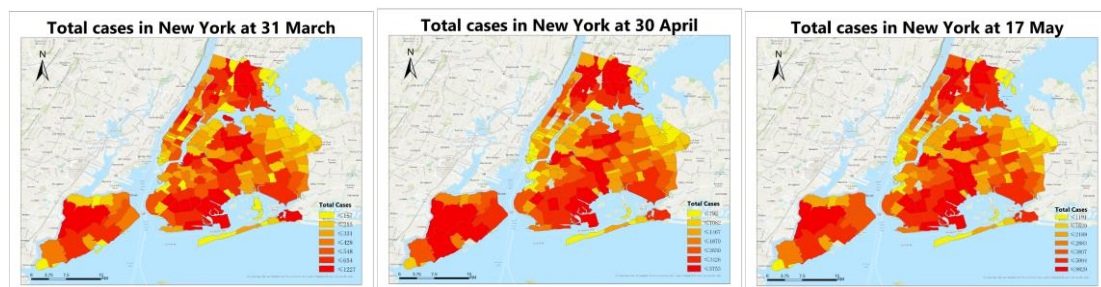

Figure 3.9: Positive cases distribution based on zip-code area in NYC (March, April, May)
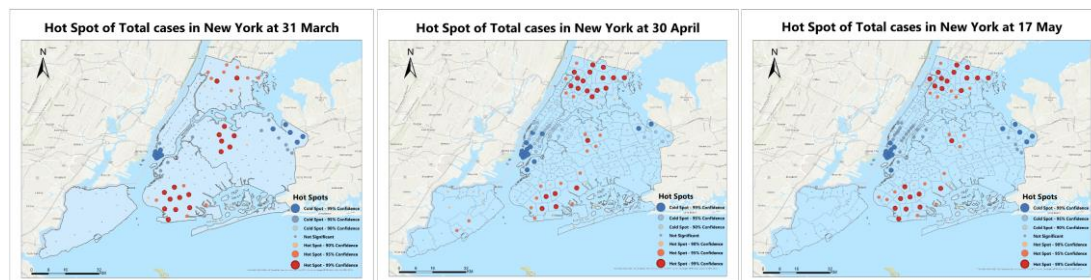

Figure 3.10: Hotspot analysis of positive cases distribution in NYC (March, April, May)

The first case relating to the COVID-19 pandemic was confirmed in New York City in March 2020. At the end of March, the infected cases increased to 33,983 at an unpredictable speed. By April, the city had more confirmed coronavirus cases than China, the U.K., or Iran, and by May, had more cases than any country other than the United States (NPR., March 24, 2020). On 20 March, the governor's office issued an executive order closing down non-essential businesses. The pause order caused the increasing unemployment rate and many social issues, whereas the infected cases of COVID-19 multiplied every day. When the city began its first phase of reopening on 8 June, the total cases had reached 211,728, accounting for 2% of the total population in NYC. From the distribution map in the zip code area, some regions hold a high infected population. To better understand the spatial correlations, the hotspot analysis was implemented. We can infer from the map that most cases clustered in Brooklyn, Bronx and the north of Queen borough.

3.2 Air quality dynamics analysis

Based on the temporal and spatial analysis of COVID-19 cases in two cities, we executed the evaluation of environmental variables including air pollutants and land surface temperature. Due to the retention of air pollutants, the air pollution dynamics is analysed monthly to compare the air quality during the COVID-19. We chose observation time span of six months. Given that the time of the outbreak in two cities is different, we evaluated the air quality data of Wuhan City and New York City from from 1st January to 30th June. The monitoring items are PM2.5, PM10, SO_2, NO_2, CO and O_3. The average air quality index (AQI) is a dimensionless index, which is calculated based on an average of six pollutants measured.

3.2.1 *Air pollutants spatio-temporal patterns in Wuhan City*

Overview of air pollutants

Figure 3.11 presents the daily concentration of the six criteria pollutants in Wuhan city from January 1st to April 30th. The daily average concentrations of $PM_{2.5}$ ranged from 8.5μg/m^3 to 108.88μg/m^3. In all 121 days, $PM_{2.5}$ in Wuhan City meet the CAAQS Grade I standard (15μg/m^3) only in 8 days, and meet the Grade II standard (35μg/m^3) in 55 days. The date of reaching the CAAQS standard (both I and II) was in quarantine period. The daily average concentrations of PM_{10} ranged from 134.54μg/m^3 to 12.88μg/m^3. In 4 months, PM_{10} exceeded the Grade I standard (40μg/m^3) for about 3 months, and exceeded the Grade II standard (70μg/m^3) for around 2 months. Monthly mean concentration of $PM_{2.5}$ decreased from 59.56μg/m^3 to 34.11μg/m^3 while monthly mean concentration of PM_{10} showed a U-shaped trend with the lowest point (69.82μg/m^3) in February and the highest point (46.03μg/m^3) in January. The high concentrations of $PM_{2.5}$ and PM_{10} reflected the fact that particular matters were still the major air pollutants during the COVID-19 epidemic.

The daily 1 h concentrations of NO_2 exceeded the Grade I & II standard (40μg/m^3, ~20ppb) for 60 days, of which only 20 days in lockdown period (from January 23rd to April 8th). NO_2 showed an abrupt decline from January 23rd to February 1st and maintained low level from February to March. This is because a series of strict prevention and control measures issued by China government led to a reduced number of vehicles on the road and diminished factory production(Bao & Zhang, 2020; X. Zhang et al., 2021).Due to the government's effectiveness of eliminating outdated production capacity and promoting clean energy, SO_2 is no longer the

major problem(H. Zhang, Di, Liu, Li, & Zhan, 2019). SO_2 meet the Grade I standard ($20\mu g/m^3$, ~7 ppb) for 103 of 121 days, and meet the Grade II standard ($60\mu g/m^3$, ~21 ppb) for all 4 months. Daily average 8 h O_3 concentrations ranged from $105.46\mu g/m^3$ to $4.46\mu g/m^3$, and daily average CO concentrations ranged from 1.56ppm to 0.47ppm. The large quarantine in China contributed to a significant decline in concentration of air pollutants except O_3. Unlike the other 5 pollutants, the concentration of O_3 showed an upward trend, increased from $33.34\mu g/m^3$ (January) to $78.78\mu g/m^3$ (April). This is because O_3 formation rate depends on the intensity of solar radiation, 8 h O_3 shows an opposite seasonal variation with the highest concentrations in the summer and the lowest in the winter(Wang, Ying, Hu, & Zhang, 2014).
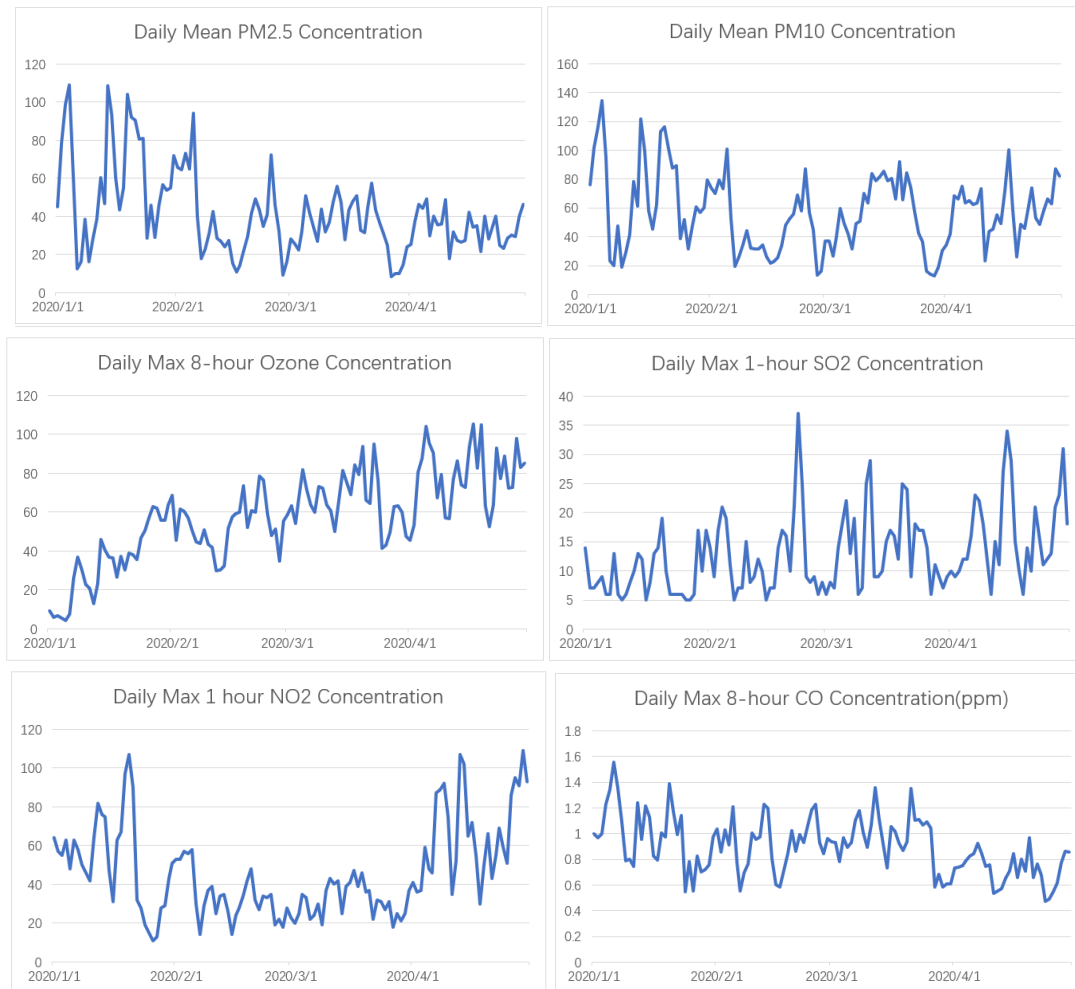

Figure 3.11: Daily mean concentrations of air pollutants: PM2.5 ($\mu g \cdot m^{-3}$), PM10 ($\mu g \cdot m^{-3}$), O_3($\mu g \cdot m^{-3}$), SO_2 ($\mu g \cdot m^{-3}$), NO_2 ($\mu g \cdot m^{-3}$), and CO (ppm) from 1st January to 31st June in Wuhan City

Spatial Analysis of air pollutants
In order to visually demonstrate of the air pollution variation, we first employed a map tool in AcGIS Pro to graphical depict the distribution of pollutants concentrations. Wuhan contains seventeen sub-districts, which concludes Jiang'an (JA), Jianghan (JH), Qiaokou (QK), Hanyang (HY), Wuhan Economic Technological Development District (WED), Hongshan (HS), East Lake High-Tech Development District (EHD), Wuchang (WC), East-Lake Ecotourism Scenic District (EES), Qingshan (QS), Wuhan Chemical Industry Park (WCIP),

Dongxihu (DXH), Xinzhou (XZ), Huangpi (HP), Jiangxia (JX), Caidian(CD), and Hannan(HN). As illustrated in Figure 7-Figure 14, the spatial-temporal distribution of different air pollutants was significantly heterogeneous among districts. Specifically, the concentrations of five air pollutants during the lockdowns appeared to be much lower than concentrations on regular days, which offered supportive evidence of the pollution reduction effects of travel restrictions.

The spatial distribution of six criteria pollutants in Wuhan City from January 2020 to June 2020 is shown in figure 7- figure 14. The concentrations of CO and NO_2 have the geographical feature of "low outside and high inside". JH and WC, which belong to the central urban area of Wuhan City, were the area with the most serious CO and NO_2 pollution because of developed traffic and large traffic volume. $PM_{2.5}$ and PM_{10} are the highest in QS District because the petroleum and power generation industries in QS District are very developed. Unlike CO and NO_2, the concentration of O_3 and SO_2 at rural area is higher than that at central area. Especially, high concentrations for O_3 and SO_2 were noticed in the northern part and southern part respectively. This is because the high vegetation rate of suburbs can release a large amount of VOCs, which is conducive to O3 production. At the same time, the NO emitted by vehicles can react with O_3, which is equivalent to consuming O_3 to a certain extent.

CO distribution in WuHan City from January to June 2020
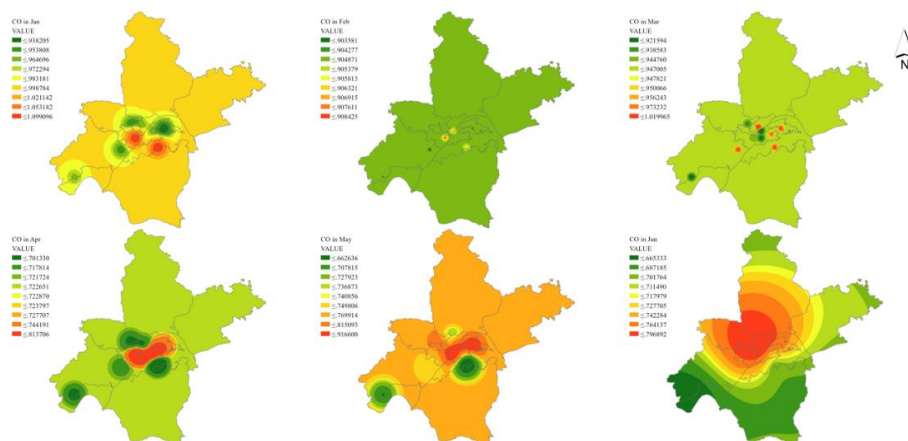
NO2 distribution in WuHan City from January to June 2020
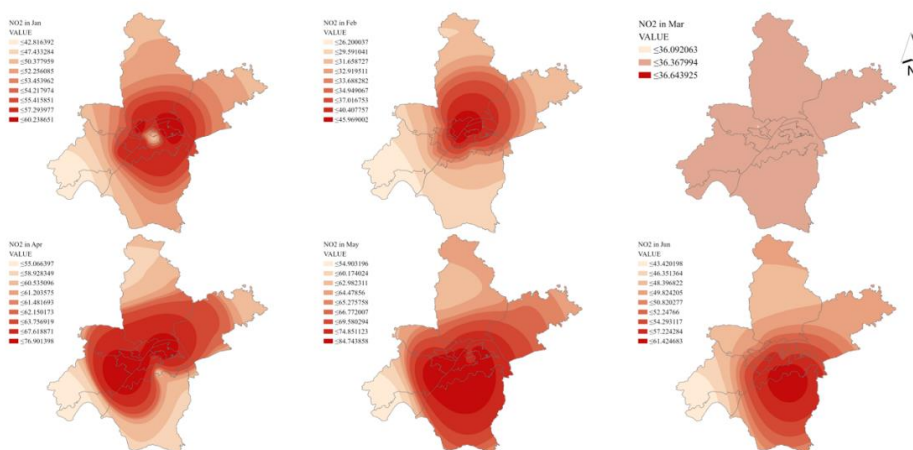
PM2.5 distribution in WuHan City from January to June 2020

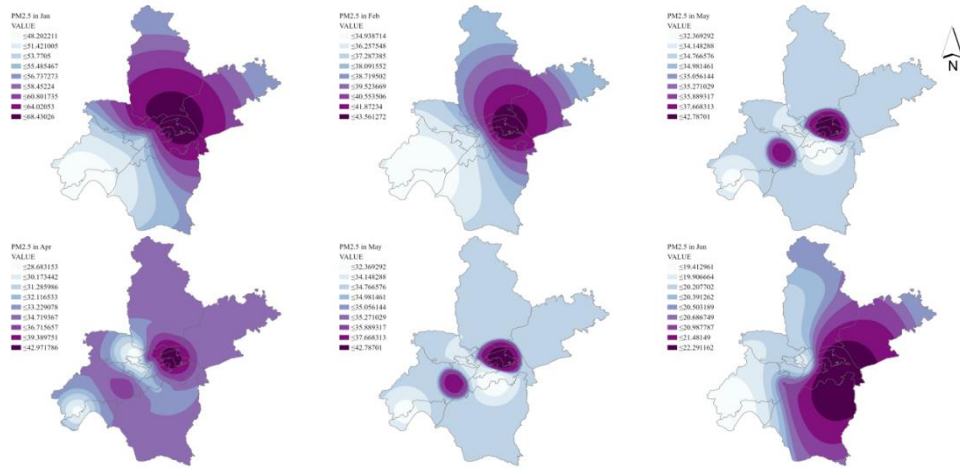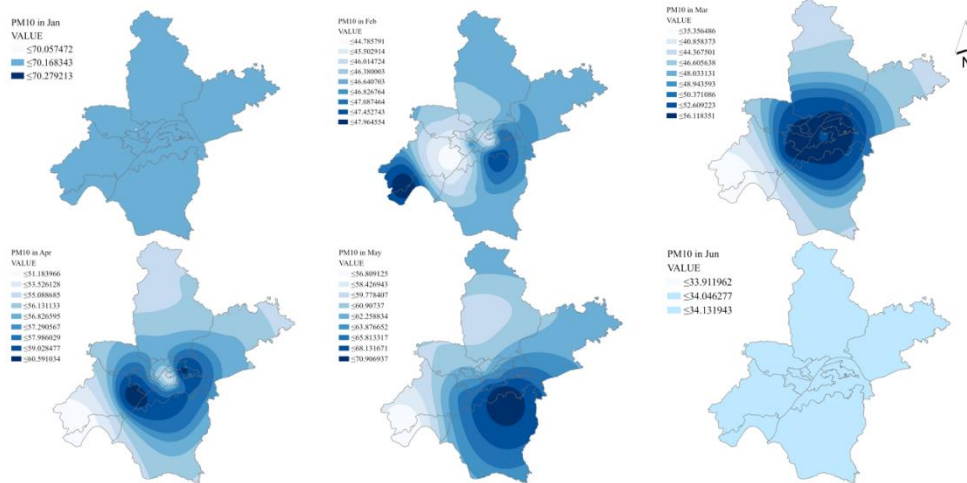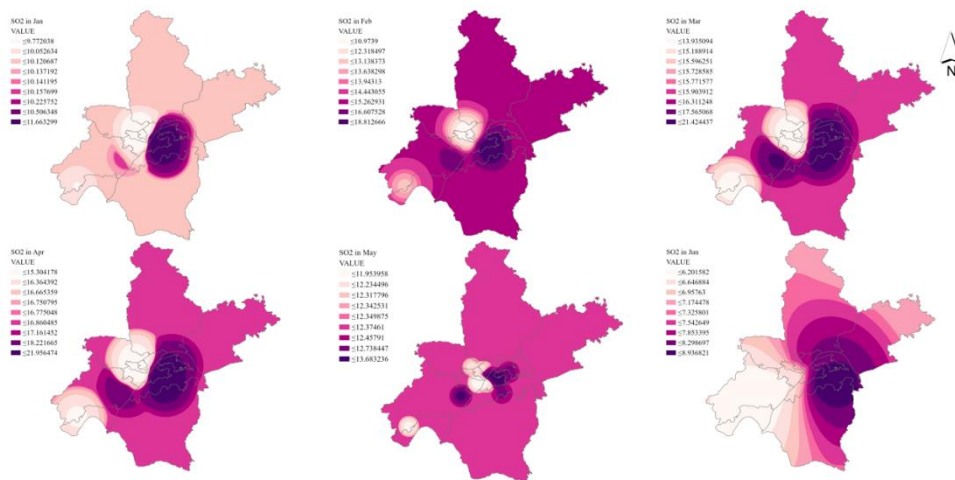# PM10 distribution in WuHan City from January to June 2020

SO2 distribution in WuHan City from January to June 2020

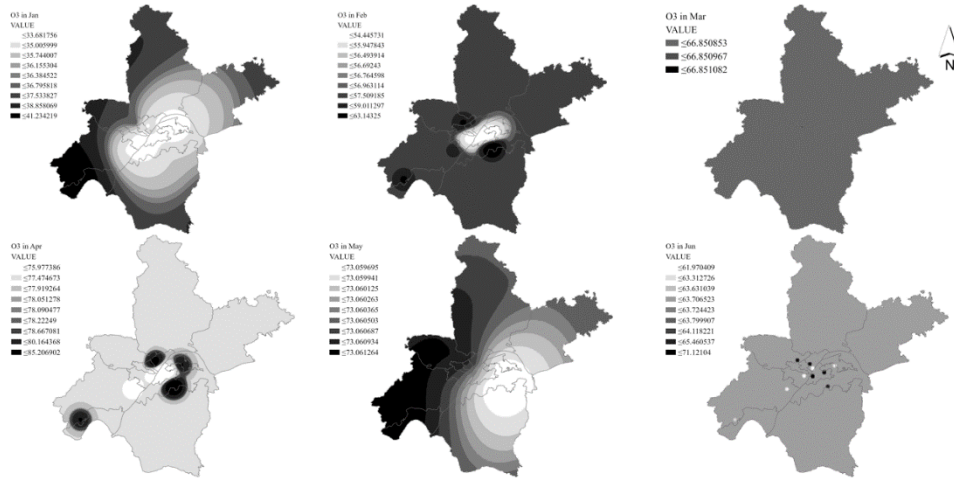O3 distribution in WuHan City from January to June 2020

Figure 3.12: Spatial Interpolation map of monthly mean concentrations of air pollutants: PM2.5 (μg · m^{-3}), PM10 (μg · m^{-3}), O$_3$(μg · m^{-3}), SO$_2$ (μg · m^{-3}), NO$_2$ (μg · m^{-3}), and CO (ppm) from 1st January to 31st June in Wuhan City

3.2.2 *Air pollutants spatio-temporal patterns in New York City*

Overview of air pollutants

In NYC air quality analysis, the PM10 data is missing in most sites. Therefore, the evaluation covers only five criteria air pollutants. According to Figure 3.13, the daily variations of five air pollutants present different change trend. The concentration of fine particulate matter (PM2.5) shows a tendency to decrease in the first three months and then increase. The Ozone concentration slightly goes up from 1st March while the nitrogen dioxide (NO$_2$) gradually decreases during the pandemic outbreak. The changes of SO$_2$ and CO are not significant, except some peak values occasionally occurs in May.
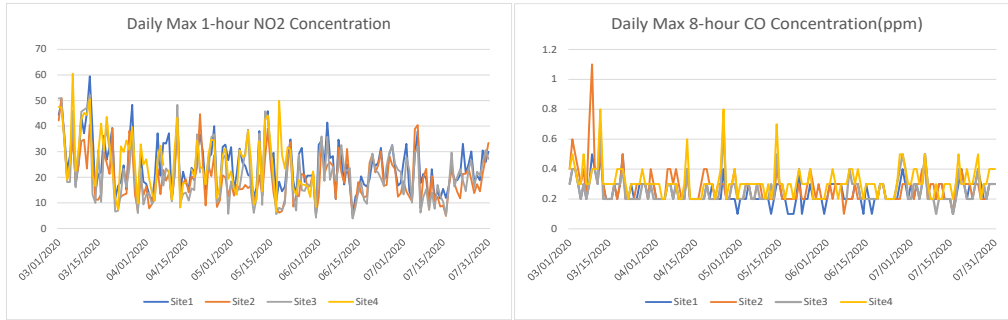

17
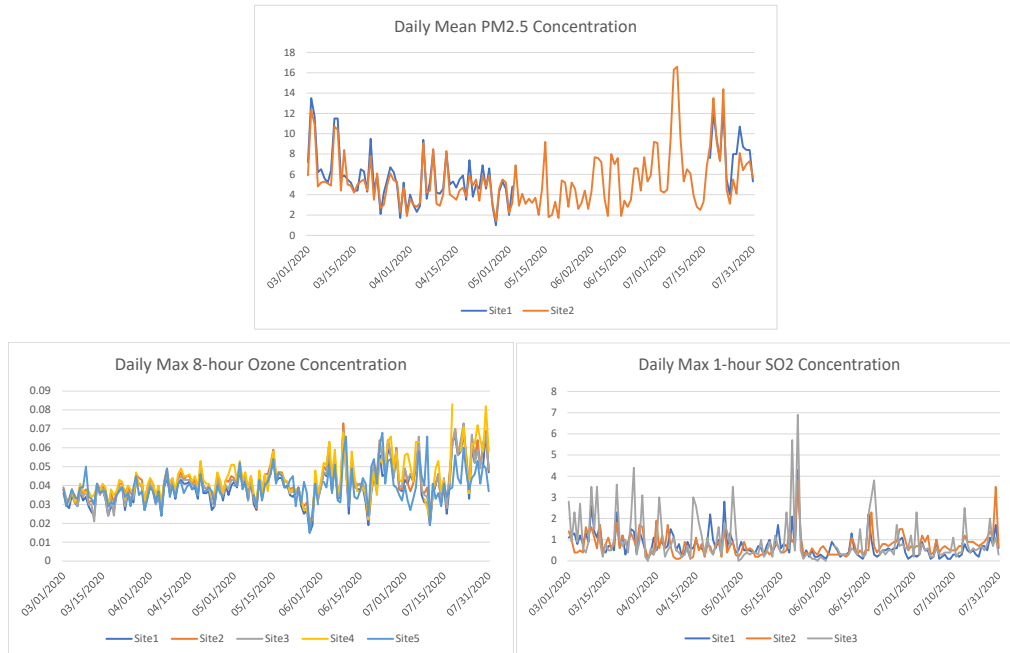
Figure 3.13: Daily average concentrations of air pollutants: PM2.5 ($\mu g \cdot m^{-3}$), PM10 ($\mu g \cdot m^{-3}$), O3($\mu g \cdot m^{-3}$), SO2 ($\mu g \cdot m^{-3}$), NO2 ($\mu g \cdot m^{-3}$), and CO (ppm) from 1st March to 31st July in New York City

Spatial Analysis of air pollutants

The monthly distribution maps of air pollutants are based on the mean values of concentration from all in-situ monitoring sites within and around the NYC urban area. The box charts (Figure 3.14) show the variation of the monthly average of PM2.5, Ozone, SO$_2$, NO$_2$, CO. The lowest point (2.28 $\mu g \cdot m^{-3}$) of PM2.5 appears in May, two months after the 'Pause Order'. The Ozone concentration ranges from 0.027 $\mu g \cdot m^{-3}$ to 0.044 $\mu g \cdot m^{-3}$, following the timeline. SO$_2$, NO$_2$ and CO present a decreasing trend from January 2020 to June 2020. The lowest point of SO$_2$ is 0.64 $\mu g \cdot m^{-3}$ in April while the highest point is 1.12 $\mu g \cdot m^{-3}$ in January. The NO$_2$ concentration varies from 22.55 $\mu g \cdot m^{-3}$ in May to 33.98 $\mu g \cdot m^{-3}$ in February, with the similar temporal variation patterns to CO. The value of CO concentration reaches the highest point (0.505 ppm) in February and lowest point in May (0.247 ppm).
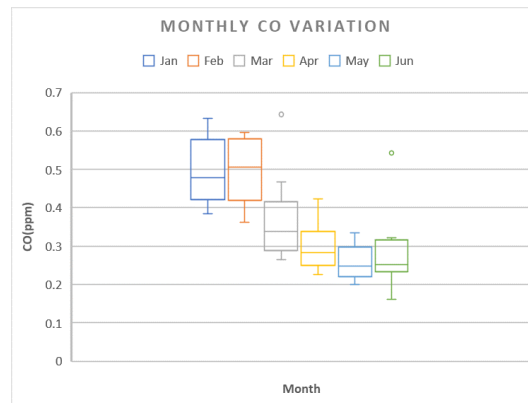

18

Figure 3.14: Monthly average concentration variation of five air pollutants: PM2.5 (μg · m^{-3}), O3(μg · m^{-3}), SO2 (μg · m^{-3}), NO2 (μg · m^{-3}), and CO (ppm) in New York City

The spatial distribution of five criteria pollutants in New York City from January 2020 to June 2020 is shown in Figure 3.15. The spatial features of pollution distribution are closely related to urban configuration and land use type. The commercial zones mostly located in Manhattan borough and industrial & manufacturing facilities are separated along the shoreside in Staten Island. The northern and eastern part of New York City like Bronx, Queens and Brooklyn are mostly residential areas.

The eastern part of NYC had lower PM2.5 concentration from February to May in 2020. After the first phase reopening order released, the PM2.5 in residential areas went higher than surrounding areas. Daily temperatures, relative humidity, and wind speed can affect ozone levels. In general, warm, dry weather is more conducive to ozone formation than cool, wet weather. NOx and VOC emissions can also influence ozone levels. The distribution of ozone displayed similar spatial patterns in March and April. In June, the centre of high density ozone moved to eastern part in the urban area.

SO$_2$, NO$_2$ and CO primarily get in the air from the burning of fuel. NO$_2$ forms from emissions from cars, trucks and buses, power plants, and industrial facilities. In NYC, the high concentration of SO2 in the atmosphere clustered in the queen borough from January to May 2020. After the pandemic outbreak, the NO$_2$ and CO pollution concentrated in Staten Island borough where most industrial facilities located.

PM2.5 distribution in New York City from January to June 2020
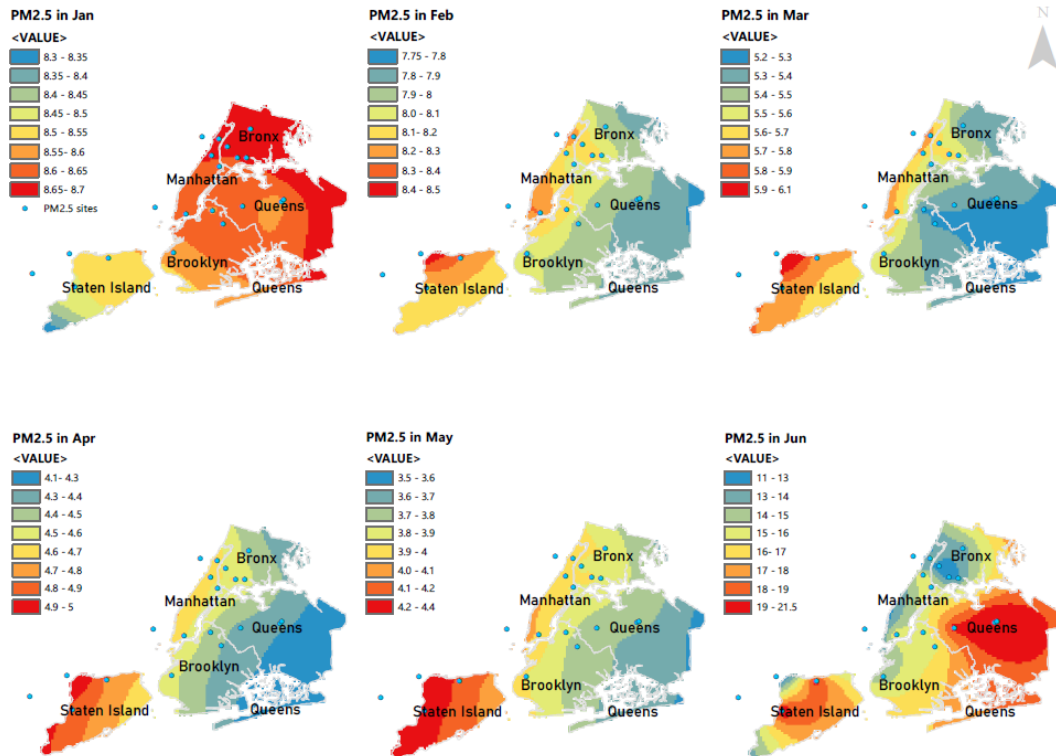
O3 distribution in New York City from January to June 2020
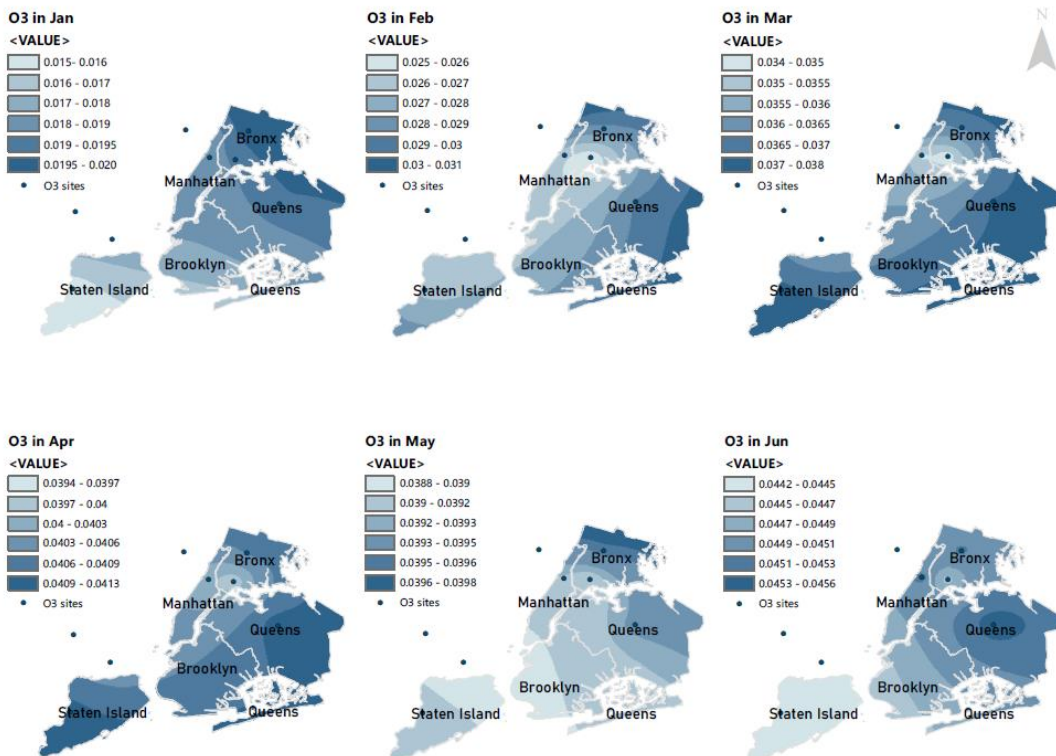
SO2 distribution in New York City from January to June 2020

NO2 distribution in New York City from January to June 2020

CO in Jan
<VALUE>
- 0.38 - 0.42
- 0.42 - 0.46
- 0.46 - 0.5
- 0.5 - 0.54
- 0.54 - 0.58
- 0.58 - 0.62
- CO sites

CO in Feb
<VALUE>
- 0.41 - 0.44
- 0.44 - 0.47
- 0.47 - 0.5
- 0.5 - 0.53
- 0.53 - 0.56
- 0.56 - 0.6
- CO sites

CO in Mar
<VALUE>
- 0.28 - 0.34
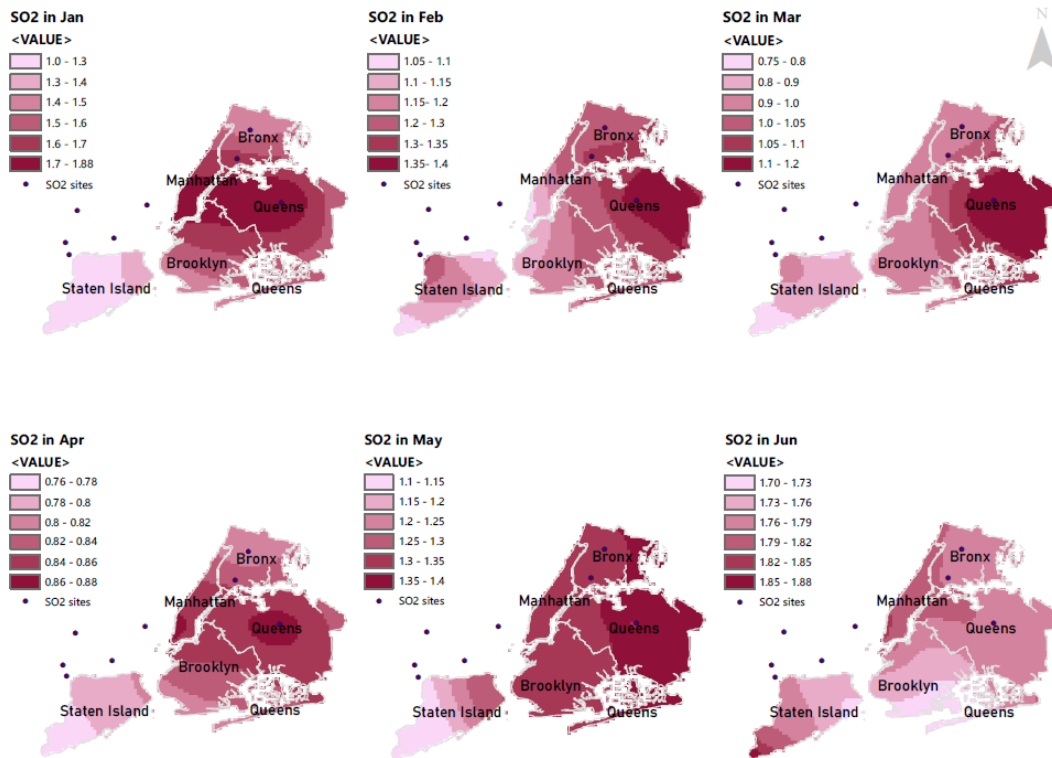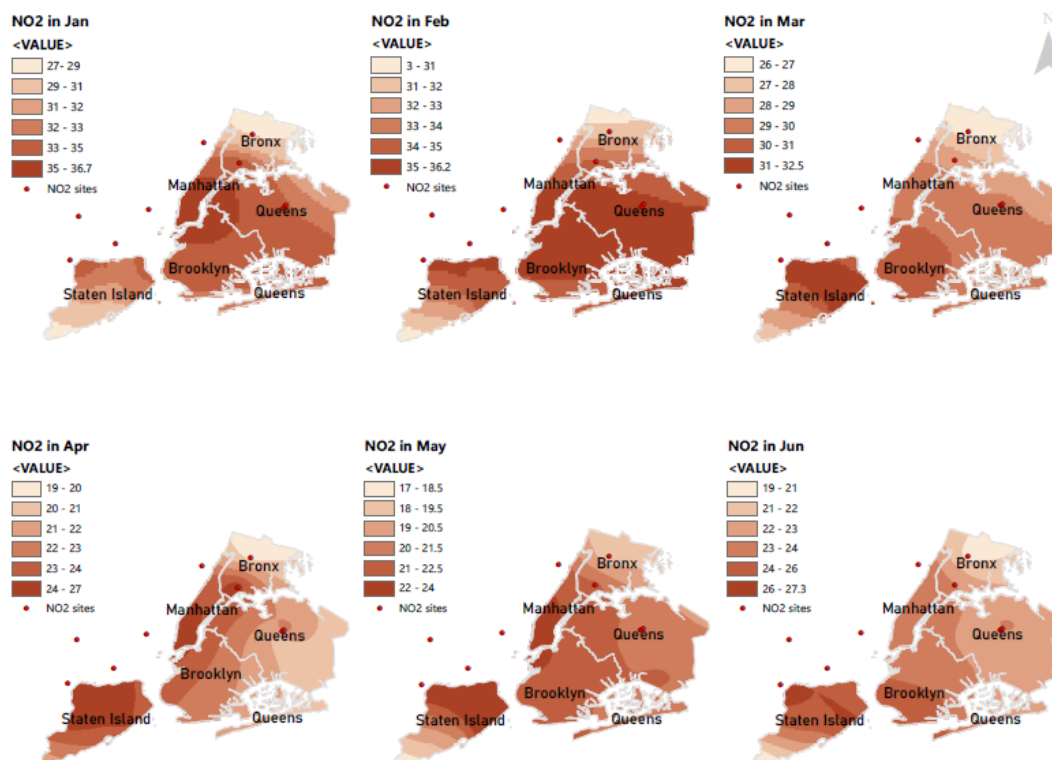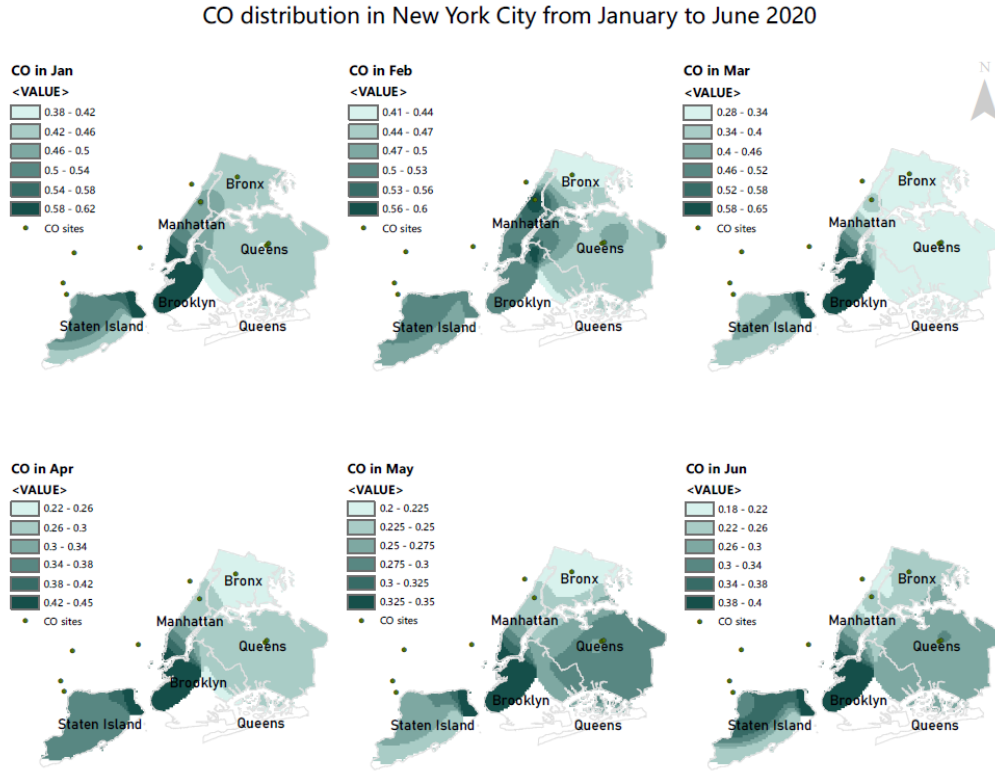- 0.34 - 0.4
- 0.4 - 0.46
- 0.46 - 0.52
- 0.52 - 0.58
- 0.58 - 0.65
- CO sites

CO in Apr
<VALUE>
- 0.22 - 0.26
- 0.26 - 0.3
- 0.3 - 0.34
- 0.34 - 0.38
- 0.38 - 0.42
- 0.42 - 0.45
- CO sites

CO in May
<VALUE>
- 0.2 - 0.225
- 0.225 - 0.25
- 0.25 - 0.275
- 0.275 - 0.3
- 0.3 - 0.325
- 0.325 - 0.35
- CO sites

CO in Jun
<VALUE>
- 0.18 - 0.22
- 0.22 - 0.26
- 0.26 - 0.3
- 0.3 - 0.34
- 0.34 - 0.38
- 0.38 - 0.4
- CO sites

Figure 3.15: Spatial interpolation map of monthly mean concentrations of air pollutants: PM2.5 ($\mu g \cdot m^{-3}$), PM10 ($\mu g \cdot m^{-3}$), O_3($\mu g \cdot m^{-3}$), SO_2 ($\mu g \cdot m^{-3}$), NO_2 ($\mu g \cdot m^{-3}$), and CO (ppm) from 1st January to 31st June in New York City

### 3.3 Urban Heat Island effects during pandemic time

In order to evaluate the impacts of COVID-19 on the urban thermal environment, the temporal maps of LST distribution are produced to make a comparison between 2019 and 2020. Generally, the UHI effect is more significant in summer because of the higher temperature and more CO_2 emissions generated from air-conditioning usage.

Wuhan City, known as one of the 'Stove City' in China, has obvious UHI effects in central urban area. From the figure 3.16(a), the distribution patterns of LST are similar in February and March. The rural area has a higher temperature than the urban area, which is assumed as a cold island effect caused by the difference in heat emissions in the urban and rural area. Through the comparison of LST in August 2019 and 2020, we found that the UHI effect is severe in 2020. Apart from the influence of global warming, the massive work resumption after months' lockdown is likely to be one of the main causes for the increase of temperature in the urban area in Wuhan City.

Contrary to Wuhan City, the UHI effect in New York City seems to mitigate in 2020 compared with the same time in 2019. Previous studies show that the epidemic influenced normal human activities. The decreased flow in the industrial and commercial area caused lower emission of CO_2. Although the change is not significant, it is safe to conclude that the COVID-19 affected the environmental variations in Wuhan City and New York City.

22
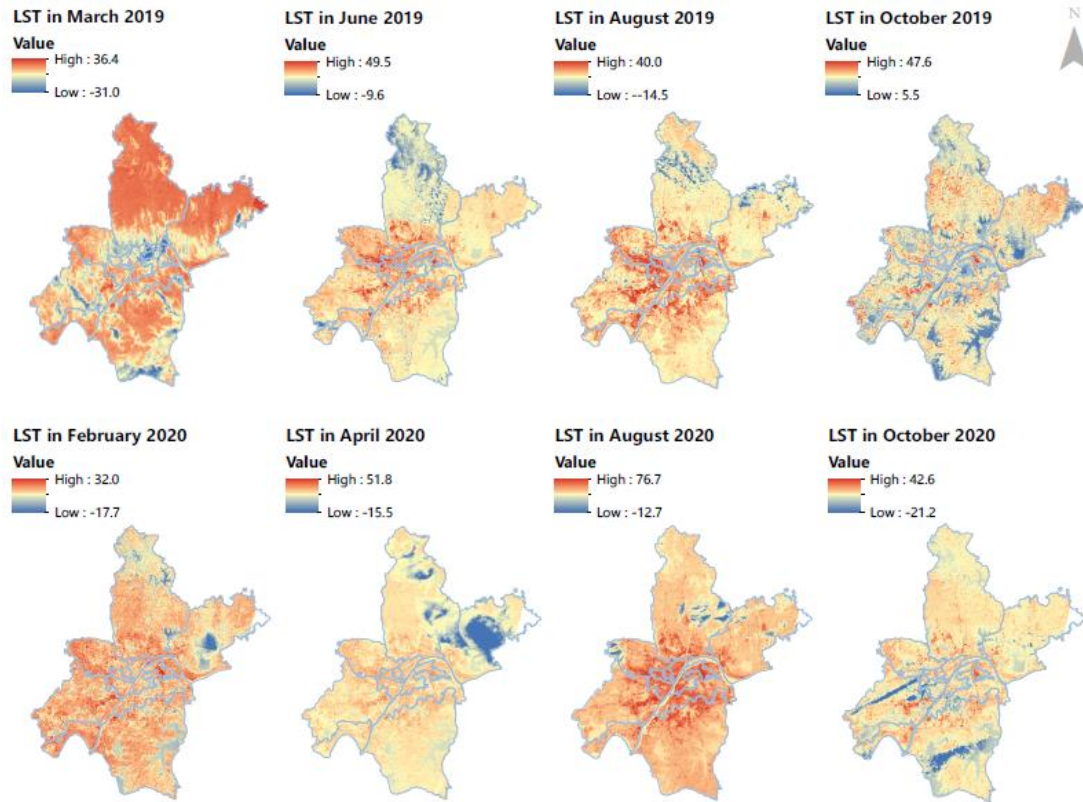
(a) Land surface temperature maps of Wuhan
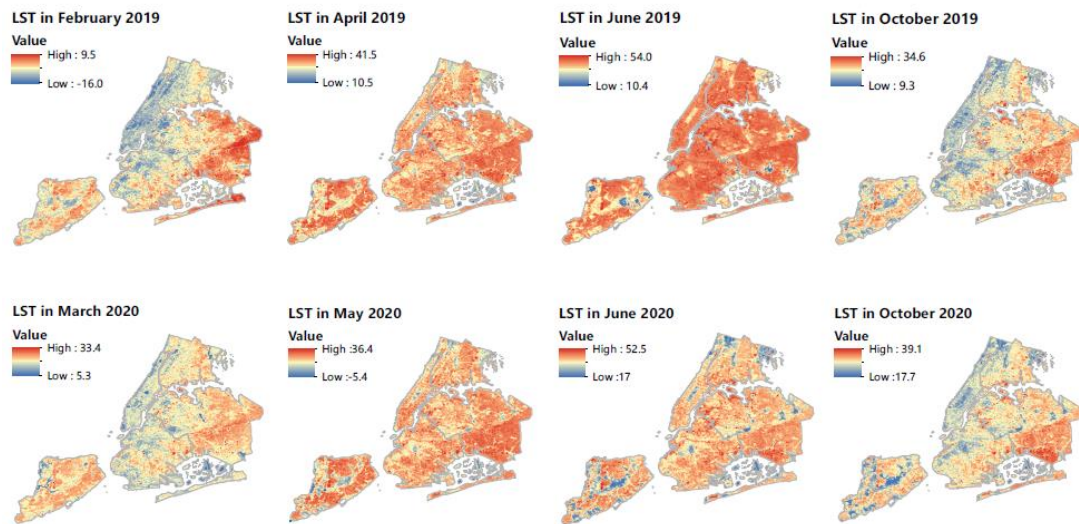
(b) Land surface temperature maps of New York City

Figure 3.16: 2019 and 2020 LST maps in Wuhan City and New York City

By calculating the Moran's I index of LST point features, it is clear that the LST has strong clustering inclination. The temperature in each location affects the adjacent location. More analysis can be conducted to study the range of the inner influence between the geographical areas in the megacities.

Table 3.1: Moran's I index of the Land Surface Temperature

	Month	Moran'I	Z-score	P-value
New York City	March	0.2433	7.733	<0.01
	May	0.3114	10.0953	<0.01
	June	0.1878	5.9727	<0.01
	October	0.2972	9.3759	<0.01
Wuhan	February	0.4239	13.0152	<0.01
	April	0.6438	20.0957	<0.01
	August	0.4554	14.4435	<0.01
	October	0.6606	20.9927	<0.01

4. Discussion

Our data and analysis demonstrate the impact of COVID-19 on environmental variations in epi-centre cities. The illustrations of dynamic changes of air pollution level and urban heat island effects in Wuhan and New York City provide information for the study of socio-ecological consequences of an epidemic outbreak. In conclusion, we found that the restrictions on human activities have positive interactions with the urban environment. The spatial-temporal patterns of air pollutants distribution were modified, especially in Wuhan City. The air quality reached the standard level due to the lockdown order. However, the resumption of industrial production and commercial activities after June 2020 brought a more severe UHI effect in central urban areas. For New York City, air pollution decreases during the outbreak time, but the change is not as significant as in Wuhan City. In addition, the UHI effects in NYC alleviated in 2020 compared with the same time in 2019. The factors contributing to the weaken UHI effects are complicated. Given the global warming tendency, the responses of the local community to COVID-19 are likely to be one of the social factors that influenced the urban thermal environment.

The limitation and future improvements in our study are as follows:
1. The correlation analysis between COVID-19 cases and air pollutants concentration was not conducted due to the limited data. With the available long-term data, we can make a more valid analysis of air quality dynamics in the pandemic period.
2. Socio-economic data and human mobility data are supposed to be prompt critical elements for the investigation of epidemic influence. In future study, these data should be taken into consideration.
3. The air and thermal factors are inseparable parts for the environmental assessment of urban context, which directly affects public health and economic development. The relationship between these two kinds of factors is another meaningful topic to study.

Our study provides insights for the research of environmental consequences of COVID-19 on a local scale. Despite the initial finding of our analysis, more correlations between critical environmental variables and disease spread can be explored in the future. Since the adaptation to long-lasting coronavirus crisis will be a new normal for human society, the statistical and quantitative analysis should be applied to assist the policy-making, economic renewal and urban environmental restoration.

5. References

Andy, M. (2005). The ESRI guide to GIS analysis, volume 2: spatial measurements and statistics.

Anselin, L. (1995). Local indicators of spatial organization -LISA. Geographical Analysis, 27(2), 93–115.

Bao, R., & Zhang, A. (2020). Does lockdown reduce air pollution? Evidence from 44 cities in northern China. Science of The Total Environment, 731, 139052. https://doi.org/https://doi.org/10.1016/j.scitotenv.2020.139052

Belkhiri, L., Tiri, A., & Mouni, L. (2020). Spatial distribution of the groundwater quality using kriging and Co-kriging interpolations. Groundwater for Sustainable Development, 11, 100473. https://doi.org/https://doi.org/10.1016/j.gsd.2020.100473

Cordes, J., & Castro, M. C. (2020). Spatial analysis of COVID-19 clusters and contextual factors in New York City. Spatial and Spatio-Temporal Epidemiology, 34, 100355. https://doi.org/10.1016/j.sste.2020.100355

Franch-Pardo, I., Napoletano, B. M., Rosete-Verges, F., & Billa, L. (2020). Spatial analysis and GIS in the study of COVID-19. A review. Science of the Total Environment, 739, 140033. https://doi.org/10.1016/j.scitotenv.2020.140033

Huang, R., Liu, M., & Ding, Y. (2020). Spatial-temporal distribution of COVID-19 in China and its prediction: A data-driven modeling analysis. Journal of Infection in Developing Countries, 14(3), 246–253. https://doi.org/10.3855/jidc.12585

Kang, D., Choi, H., Kim, J. H., & Choi, J. (2020). Spatial epidemic dynamics of the COVID-19 outbreak in China. International Journal of Infectious Diseases, 94(January), 96–102. https://doi.org/10.1016/j.ijid.2020.03.076

Kuttappan, J., & Chen, Z. (2020). Changing Social Patterns during Covid-19. July.

Li, H., Calder, C., & Cressie, N. (2007). Beyond Moran's I: Testing for Spatial Dependence Based on the Spatial Autoregressive Model. Geographical Analysis, 39, 357–375. https://doi.org/10.1111/j.1538-4632.2007.00708.x

Li, R. Y. M., Chau, K., Li, H., Zeng, F., Tang, B., & Ding, M. (2021). Remote Sensing, Heat Island Effect and Housing Price Prediction via AutoML (pp. 113–118). https://doi.org/10.1007/978-3-030-51328-3_17

Mukherjee, S., & Debnath, A. (2020). Correlation between Land Surface Temperature and Urban Heat Island with COVID-19 in New Delhi, India. 1–11. https://doi.org/10.21203/rs.3.rs-30416/v1

Nakada, L. Y. K., & Urban, R. C. (2020). COVID-19 pandemic: Impacts on the air quality during the partial lockdown in São Paulo state, Brazil. Science of The Total Environment, 139087.

NPR. March 24, 2020. New York City, U.S. Epicenter, Braces For Peak.

Ozili, P. K., & Arun, T. (2020). Spillover of COVID-19: Impact on the Global Economy. *SSRN Electronic Journal*. https://doi.org/10.2139/ssrn.3562570

Peng, Z., Wang, R., Liu, L., & Wu, H. (2020). Exploring urban spatial features of COVID-19 transmission in Wuhan based on social media data. *ISPRS International Journal of Geo-Information*, 9(6). https://doi.org/10.3390/ijgi9060402

Rodríguez-Urrego, D., & Rodríguez-Urrego, L. (2020). Air quality during the COVID-19: PM2.5 analysis in the 50 most polluted capital cities in the world. *Environmental Pollution*, *266*, 115042. https://doi.org/10.1016/j.envpol.2020.115042

Ruiz Estrada, M. (2020). *Economic Waves: The Effect of the Wuhan COVID-19 On the World Economy (2019-2020)*. https://doi.org/10.13140/RG.2.2.11861.99047/1

U.S. Census Bureau QuickFacts: New York City, New York. (2020). Retrieved May 28, 2020, from https://www.census.gov/quickfacts/newyorkcitynewyork

Wang, Y., Ying, Q., Hu, J., & Zhang, H. (2014). Spatial and temporal variations of six criteria air pollutants in 31 provincial capital cities in China during 2013–2014. *Environment International*, *73*, 413–422. https://doi.org/https://doi.org/10.1016/j.envint.2014.08.016

Wang, M., Zhang, Z., He, G., Wang, G., Long, T., & Peng, Y. (2016). An enhanced single-channel algorithm for retrieving land surface temperature from Landsat series data. Journal of Geophysical Research: Atmospheres, 121(19), 11,712-11,722. https://doi.org/10.1002/2016JD025270

Yang, Q., Huang, X., & Tang, Q. (2019). The footprint of urban heat island effect in 302 Chinese cities: Temporal trends and associated factors. Science of the Total Environment, 655, 652–662. https://doi.org/10.1016/j.scitotenv.2018.11.171

Yuan, Li (28 January 2020). "Coronavirus Crisis Exposes Cracks in China's Facade of Unity". The New York Times. ISSN 0362-4331.

Zhang, H., Di, B., Liu, D., Li, J., & Zhan, Y. (2019). Spatiotemporal distributions of ambient SO2 across China based on satellite retrievals and ground observations: Substantial decrease in human exposure during 2013–2016. *Environmental Research*, *179*, 108795. https://doi.org/https://doi.org/10.1016/j.envres.2019.108795

Zhang, X., Estoque, R. C., & Murayama, Y. (2017). An urban heat island study in Nanchang City, China based on land surface temperature and social-ecological variables. Sustainable Cities and Society, 32(May), 557–568. https://doi.org/10.1016/j.scs.2017.05.005

Zhang, X., Tang, M., Guo, F., Wei, F., Yu, Z., Gao, K., Jin, M., Wang, J., & Chen, K. (2021). Associations between air pollution and COVID-19 epidemic during quarantine period in China. *Environmental Pollution*, *268*, 115897. https://doi.org/https://doi.org/10.1016/j.envpol.2020.115897